Modulating Skeletons of Covalent Organic Framework for High-Efficiency Gold Recovery

Minghao Liu,[a] [b]+ Di Jiang, [c] [d]+ Yubin Fu,[e]+ George Zheng Chen, [f] Shuai Bi,[g] Xuesong Ding,[c]* Jun He,[b] [h] Bao-Hang Han, [c] [d] Qing Xu [a] [i]* and Gaofeng Zeng[a] [i]*

[a]   M. Liu, Prof. Q. Xu, Prof. G. Zeng,
CAS Key Laboratory of Low-Carbon Conversion Science and Engineering
Shanghai Advanced Research Institute (SARI), Chinese Academy of Sciences (CAS)
Shanghai 201210, P. R. China
E-mail: xuqing@sari.ac.cn; zenggf@sari.ac.cn

[b]   M. Liu, Prof. J. He,
Department of Chemical and Environmental Engineering
University of Nottingham Ningbo China
Ningbo, 315199, P.R. China

[c]   D. Jiang, Prof. X. Ding, Prof. B.-H. Han,
CAS Key Laboratory of Nanosystem and Hierarchical Fabrication
CAS Center for Excellence in Nanoscience
National Center for Nanoscience and Technology, Beijing 100190, China
E-mail: dingxs@nanoctr.cn

[d]   D. Jiang, Prof. B.-H. Han,
Sino-Danish Center for Education and Research
Sino-Danish College University of Chinese Academy of Sciences
Beijing 100049, P. R. China

[e]   Dr. Y. Fu,
Center for Advancing Electronics Dresden (cfaed) & Faculty of Chemistry and Food Chemistry
Technische Universität Dresden
Dresden, 01062, Germany

[f]   Prof. G. Z. Chen,
Department of Chemical and Environmental Engineering
University of Nottingham
Nottingham, NG7 2RD, UK

[g]   Dr. S. Bi,
School of Chemistry, Chemical Engineering and Biotechnology
Nanyang Technological University
21 Nanyang Link, Singapore, 637371, Singapore

[h]   Prof. J. He,
Nottingham Ningbo China Beacon of Excellence Research and Innovation Institute
University of Nottingham
Ningbo 315100, China

[i]   Prof. Q. Xu, Prof. G. Zeng,
School of Chemical Engineering Beijing 100049
University of Chinese Academy of Sciences

Beijing 100049, China

[+] These authors equally contributed this work.

Supporting information for this article is given via a link at the end of the document.

Abstract: Covalent organic frameworks (COFs) have attracted considerable attention as adsorbents for capturing and separating gold from electronic wastes. To enhance the binding capture efficiency, constructing hydrogen-bond nanotraps along the pore walls was one of the most widely adopted approaches. However, the development of absorbing skeletons was ignored due to the weak binding ability of the gold salts (Au). Herein, we demonstrated skeleton engineering based on diarylamine derivatives to construct highly efficiently absorbs for Au capture. The strong electronic donating feature of diarylamine units enhanced the electronic density of binding sites (imine-linkage) and thus resulted in a high capacity of over 1750 mg g^{-1} for all three COFs. Moreover, the absorbing performance was further improved via the ionization of diarylamine units. The ionic COF achieved 90% of the maximal adsorption capacity, 1.63 times of that from the charge-neutral COF within ten minutes, and showed remarkable uptakes of 1834 mg g^{-1}, exceptional selectivity (97.45%) and cycling stability. The theoretical calculation revealed the binding sites altering from imine bonds to ionic amine sites after ionization of the frameworks, which enabled to bind the AuCl$_4^-$ via coulomb force dispensing with protonation imine bond process and contributed to enhanced absorbing kinetics. This work inspires us to design molecular/ionic capture based on COFs.

Introduction

Gold (Au), as one of the precious metals, is a fundamental and high-value resource.[1] Au is widely applied in electronic devices, catalysis and the jewelry industry owing to its excellent chemical and physical properties.[2] However, the increased consumption and demand for gold led to a requirement of production and recycling. To date, the leach solution and e-waste, containing the content of gold at ~2000 ppm, are much richer than that in natural mines (about 30 ppm).[3] In addition, both of natural mines and e-waste contained many competitive metals including copper, cadmium, chromium, aluminum and cobalt, further leading to the difficulty and high energy consumption in the extraction process.[4] Therefore, it is vital to construct a selective and reusable gold-ion adsorbent with high capture efficiency and capacity.

Covalent organic frameworks (COFs), as an emerging class of crystalline porous organic materials, are constructed by building blocks through covalent bonds.[5] Compared with other organic polymers, COFs exhibit well-defined frameworks, controllable porosities, excellent chemical stabilities, and results in designable functions, and these features endowed COFs with various applications in molecular / gas absorption, electro- / photo-catalysis, conversion systems and chemical sensing.[6-7] COFs have the potential to cater to the requirements of the extraction due to their elaborate designability and modifiability.[8] Introducing binding groups along the pore walls of COFs has been shown to capture various ions such as Hg^{2+}, UO_2^{2+}, and Cr^{4+}.[9] Specifically, several COFs with different functional groups were proposed to endow COFs with specific recognition and high uptakes for gold ions via H-bond interaction.[10] Most COFs for Au capture focused on modifying the porous walls with specified groups (e.g., thiol, phenolic and amide groups) to construct H-bond traps to capture Au.[11] However, the development of frameworks was ignored because of the weak binding ability of the Au ions. Recently, the C=N linkages in non-interpenetration three-dimensional COF were adopted for gold recovery but with a low capacity of 570.18 mg g^{-1}.[12] Thus, it is a challenge to construct absorbing frameworks for high-capacity and rapid Au capture.

Herein, we demonstrated the skeleton engineering of COFs to construct highly efficient Au absorption (Scheme 1A). With introducing diarylamine derivatives into frameworks, the electron density of the C=N linkages was enhanced, which contributed to highly capacitive Au capture, with Au uptakes over 1750 mg g^{-1} for three synthesized COF. Furthermore, the diarylamine can be ionized, which enables the binding Au ions via coulomb force rather than H-bond and contributes fast kinetic performance, achieving high efficiency (90% adsorption of maximum capacity in 10 mins).

Results and Discussion

The targeted COFs were synthesized by the diarylamine derivatives (Scheme 1B) and

4,4',4",4'''-(pyrene-1,3,6,8-tetrayl)tetraaniline (PYTA). The different length including 4,4',4",4'''-(1,4-phenylenebis(azanetriyl))tetrabenzaldehyde (PATA), 4,4',4",4'''-([1,1'-biphenyl]-4,4'-diylbis(azanetriyl))tetrabenzaldehyde (BDTA) and 4,4',4",4'''-([1,1':4',1"-terphenyl]-4,4"-diylbis(azanetriyl))tetrabenzaldehyde (TDTA) were employed to construct PYTA-PATA-COF, PYTA-BDTA-COF and PYTA-TDTA-COF. All three charge-neutral COFs were synthesized with the mixed solvents (1,2-dichlorobenzene / benzyl alcohol) with 6.0 M HOAc as the catalyst at 120 °C for 72 hours, and the corresponding yields were 86.5, 78.3 and 82.4%, respectively. To enhance the binding affinity of the skeletons toward $AuCl_4^-$, we take PYTA-PATA-COF with the highest surface areas among the synthesized three COFs as an example to construct an ionic skeleton by using the Menshutkin reaction for gold recovery performance (Scheme 1C). Methyl iodide was adopted to ionize the frameworks because of its high activity towards the Menshutkin reaction.[13]
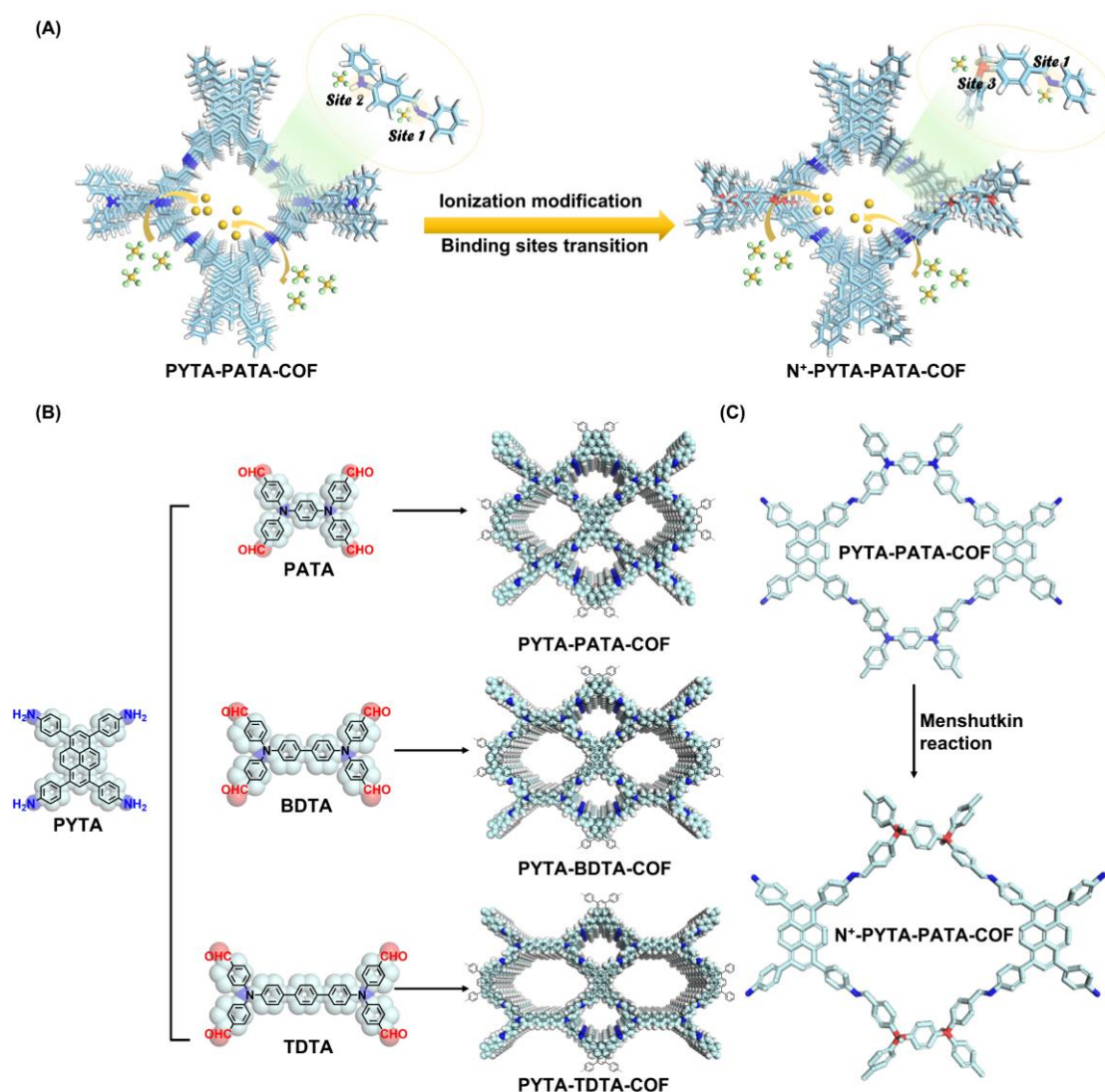
Scheme 1. (A) The scheme for the transition of the binding sites after the ionization modification over COFs for Au recovery. (B) Synthesis of PYTA-PATA-COF, PYTA-BDTA-COF and PYTA-TDTA-COF from PYTA, PATA, BDTA and TDTA building units. (C) The synthesis of N⁺-PYTA-PATA-COF by the Menshutkin reaction.

The crystal structures for as-synthesized COFs are investigated using powder X-ray diffraction (PXRD).[14] The PXRD patterns for PYTA-PATA-COF showed that peaks from (100), (110), (220), (310) and (001) facets were at 3.29, 5.55, 7.77, 16.31, and 21.2°, respectively (Figure 1A). The Pawley refinements reveal the theoretical structures were in accordance with the experimental results with Rwp and Rp of 3.12 and 2.07%, respectively (Table S1-S2). The COF adopted P1 space groups with a = 25.2006 Å, b = 23.4168 Å, c = 3.7577 Å, and the corresponding $\alpha = \beta = \gamma = 90°$.

According to the simulation method in Materials Studio, the AB stacking modes of PYTA-PATA-COF did not match the experimental results (Figures 1D and S1). Thus, PYTA-PATA-COF was stacked in the AA stacking model. The PYTA-BDTA-COF demonstrated peaks at 5.32, 6.30, 7.85 and 10.54° due to the (110), (200), (101) and (211) facets, with the Rwp and Rp of 4.21 and 3.10%, respectively (Figure 1B). The PYTA-BDTA-COF adopted I222 space groups with a = 28.0243 Å, b = 22.4871 Å, c = 12.3095 Å, and the corresponding α = β = γ = 90° (Tables S3-S5). Meanwhile, the AA staggered stacking model was in accordance with the PYTA-BDTA-COF instead of the eclipsed AA and AB stacking modes of PYTA-BDTA-COF (Figures 1E and S2-S3). Furthermore, PYTA-TDTA-COF also exhibited a good crystallinity with intense peaks at 3.31, 3.82, 5.35, 8.24, 12.04, 16.43 and 21.96° from (010), (110), (210), (120), (320), (230) and (001) (Figure 1C and Tables S6-S7). Correspondingly, the PYTA-TDTA-COF adopted AA stacking modes instead of the AB stacking model (Figures 1F and S4). In addition, the crystal structure of the N^+-PYTA-PATA-COF well remained after the ionic modification, with peaks of (100), (110), (220) and (001) at 3.42, 5.66, 7.87 and 21.66°, respectively (Figure 1A and Tables S8-S9).
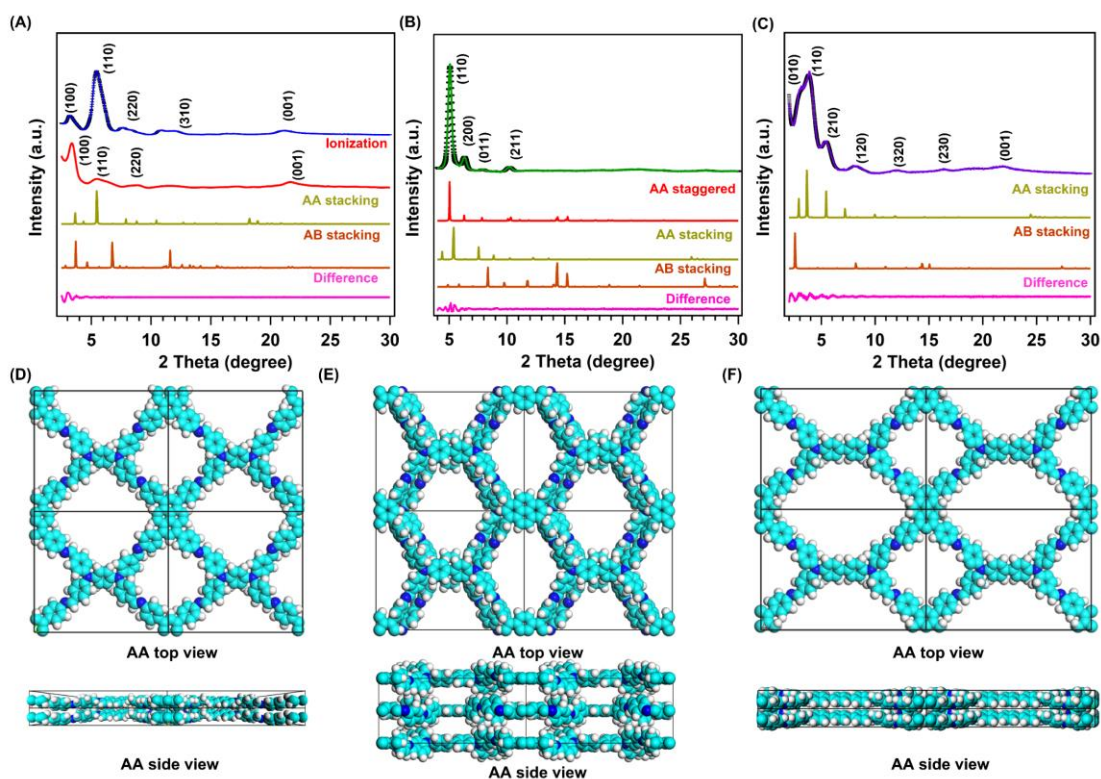
Figure 1. The PXRD profiles for (A) PYTA-PATA-COF of the experimentally observed

(blue), Pawley refined (black), simulated using the AA (yellow), AB (orange) stacking modes, difference (pink) and experimental PXRD pattern of N^+-PYTA-PATA-COF (red). The PXRD profiles for (B) PYTA-BDTA-COF and (C) PYTA-TDTA-COF of the experimentally observed, Pawley refined (black), simulated using the AA staggered (red), AA (yellow) and AB (orange) stacking modes and difference (pink). The theoretically unit cells of the AA stacking modes for (D) PYTA-PATA-COF, (E) PYTA-BDTA-COF and (F) PYTA-TDTA-COF, respectively.

The Schiff-based condensation reaction and the ionic modification were verified using the Fourier transform infrared spectroscopy (FT IR). Specifically, the strong vibration bonds from C=N linkages were at around 1620 cm^{-1}, indicating successful synthesis of the COFs (PYTA-PATA-COF, PYTA-BDTA-COF and PYTA-TDTA-COF) (Figure S5).[15] In addition, the peaks from the C-N linkage were also identified at around 1105 cm^{-1} for these COFs (Figure S5).[13e] After the ionic modification, the C=N bonds were maintained and a new peak appeared at 910 cm^{-1} from the $-N^+$-$(CH_3)_2^-$ bonds of N^+-PYTA-PATA-COF, further revealing that the ionization of the skeleton by the Menshutkin reaction (Figure S6).[16] The chemical structures of these COFs (PYTA-PATA-COF, PYTA-BDTA-COF and PYTA-TDTA-COF) were further confirmed by using the solid ^{13}C solid-state nuclear magnetic resonance (^{13}C NMR) (Figure 2A). The characteristic signals at around 154 ppm can be assigned to –C=N of PYTA-PATA-COF, PYTA-BDTA-COF and PYTA-TDTA-COF, confirming the success of the condensation reaction (Figure 2A). Additionally, the peaks at ~145 ppm corresponded to the carbon atoms of C-N for PYTA-PATA-COF, PYTA-BDTA-COF and PYTA-TDTA-COF. Meanwhile, the peaks from 110 to 140 ppm were assigned to the carbon atoms of the benzene units for these COFs. In addition, N^+-PYTA-PATA-COF demonstrated that a new peak appeared at 67 ppm (Figure 2A, red curve), assigning to methyl groups, indicating the successful Menshutkin reaction.[6c]

The porous structures of COFs are crucial for the ion adsorption. The N_2 physisorption behaviors of PYTA-PATA-COF, PYTA-BDTA-COF, PYTA-TDTA-COF and N^+-

PYTA-PATA-COF were studied at 77 K. These COFs exhibited a steep increase in the N_2 adsorption–desorption isotherms at P/P_0 around 0, which was due to the filling of micropores, revealing a pore shrinkage. Specifically, PYTA-PATA-COF showed a Brunauer–Emmett–Teller (BET) surface area (S_{BET}) of 1063.08 m^2 g^{-1} (Figure 2B, blue curve). The corresponding S_{BET} values for PYTA-BDTA-COF, PYTA-TDTA-COF and N^+-PYTA-PATA-COF were 492.72, 835.37 and 735.15 m^2 g^{-1}, respectively (Figure 2B). And the pore size distribution curve for PYTA-PATA-COF showed the pore sizes were 1.28 and 1.52 nm, with a total pore volume of 0.84 cm^3 g^{-1} (Figure 2C). PYTA-BDTA-COF, PYTA-TDTA-COF and N^+-PYTA-PATA-COF had dual porous structures and delivered the pore volumes of 0.64, 0.73 and 0.66 cm^3 g^{-1}, respectively. (Figures 2D-2F). The pore sizes for the PYTA-BDTA-COF, PYTA-TDTA-COF and N^+-PYTA-PATA-COF located at 1.55/1.81, 1.14/1.61/1.81 and 1.29/1.54 nm, respectively.
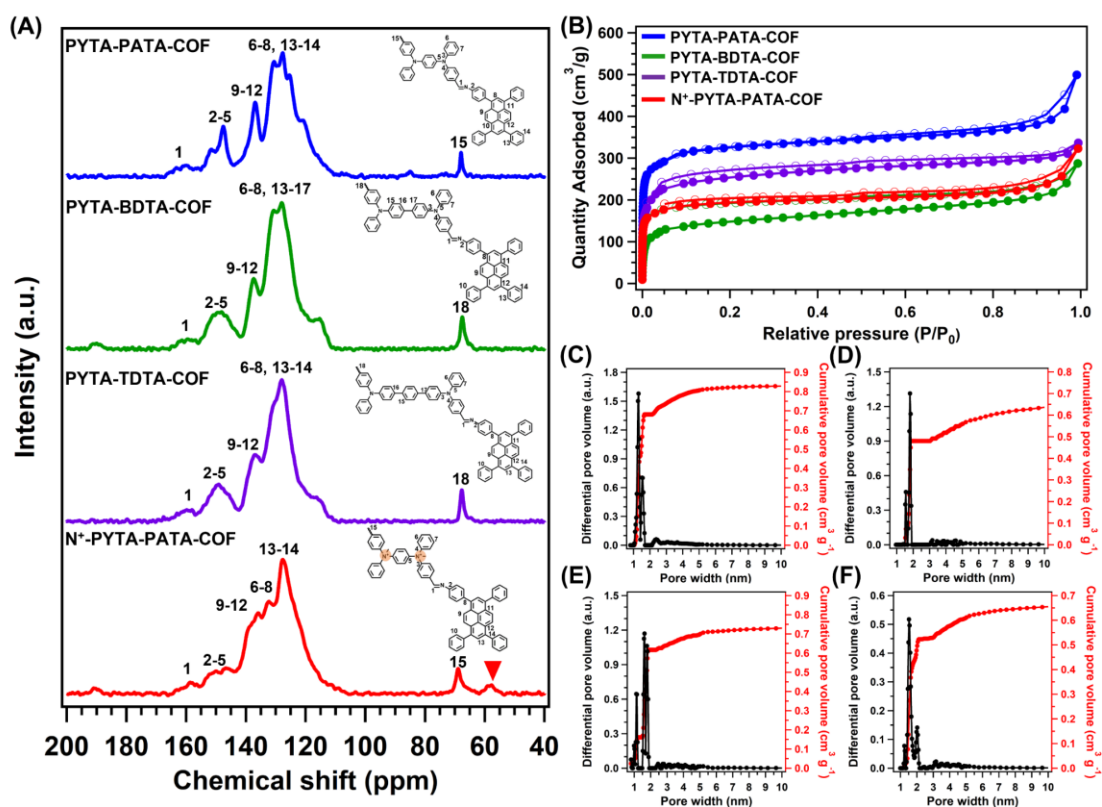
Figure 2. (A) The ^{13}C NMR spectra and (B) N_2 adsorption curve at 77 K of PYTA-PATA-COF (blue), PYTA-BDTA-COF (green), PYTA-TDTA-COF (purple) and N^+-PYTA-PATA-COF (red), respectively. The pore distribution curves of (C) PYTA-PATA-

COF, (D) PYTA-BDTA-COF, (E) PYTA-TDTA-COF and (F) N^+-PYTA-PATA-COF, respectively.

The atom states and coordination of these COFs were confirmed via X-ray photoelectron spectroscopy (XPS). As shown in Figure 3A, the high-resolution N 1s spectra of PYTA-PATA-COF, PYTA-BDTA-COF and PYTA-TDTA-COF indicated two peaks at around 399.71 and 400.98 eV for C=N from imine bonds and C-N from diarylamine derivatives, respectively. After introducing the ionization skeleton, the new peak at 402.33 eV was assigned to $C-N^+$ bonds of N^+-PYTA-PATA-COF, further suggesting the successful ionic modification (Figure 3A, red curve). Furthermore, the grafting rate of the ionic groups ranged from 71% to 74%, respectively, determined by the content of I^- and $C-N^+$ (Figure S7 and Tables S10-S11). Moreover, the Zeta potential verified the charge position of these COFs. Specifically, the Zeta potential of PYTA-PATA-COF, PYTA-BDTA-COF, PYTA-TDTA-COF and N^+-PYTA-PATA-COF were -0.58, -6.82, -0.84 and 20.57 mV, respectively, further suggesting the superior electrostatic interaction between N^+-PYTA-PATA-COF and ions (Figure 3B).

The chemical and thermal stabilities of these COFs were then investigated. All the synthesized COFs were stable in many organic solvents (DMF, DMSO and $CHCl_3$), 1 M HCl, 1 M NaOH and pure water for one week as revealed by the PXRD patterns. The residue weight percentage of these COFs confirmed their chemical stability (remained over 98%, Figures S8-S12 and Table S12). However, these COFs showed partly decomposition in harsh conditions, including aqueous HCl (6 M) and aqueous NaOH (6 M) solutions, with residual weight percentages of over 70 and 90 wt.%, and lower intensities as revealed by the PXRD patterns (Figure S12 and Table S12).

In addition, thermogravimetric analysis (TGA) measurements are conducted to confirm the thermal stability under the N_2 atmosphere. TGA curves revealed that no obvious observation of the decomposition for PYTA-PATA-COF, PYTA-BDTA-COF and PYTA-TDTA-COF at < 500 °C under the N_2 atmosphere (Figure S13). For the N^+-

PYTA-PATA-COF, TGA curves illustrated an obvious decomposition due to the existence of CH_3I. In addition, the TGA curves demonstrated that the N^+-PYTA-PATA-COF left at 9.5 % after 660 °C under air (Figure S14). These results indicated that these COFs displayed good chemical and thermal stability.

The contact angle of water on PYTA-PATA-COF, PYTA-BDTA-COF, PYTA-TDTA-COF and N^+-PYTA-PATA-COF were conducted. As shown in Figure S15, the measured contact angles of PYTA-PATA-COF, PYTA-BDTA-COF, PYTA-TDTA-COF and N^+-PYTA-PATA-COF were 78, 127, 137 and 93 °, suggesting that the introduction of benzene rings and methyl groups would bring the hydrophobic behavior.

Scanning electron microscopy (SEM) and transmission electron microscopy (TEM) were measured to confirm the morphology of PYTA-PATA-COF, PYTA-BDTA-COF, PYTA-TDTA-COF and N^+-PYTA-PATA-COF. The SEM images showed that PYTA-PATA-COF was composed of microcrystalline particles with around 100 nm in diameter (Figure S16). The SEM images of N^+-PYTA-PATA-COF also illustrated the identical microcrystalline particles, suggesting the post-modification did not change the morphology (Figure S17). In addition, the SEM images exhibited that PYTA-BDTA-COF had a bar shape composed of sheets with a width of 20 nm and a length of 240 nm (Figure S18). The SEM images of PYTA-TDTA-COF exhibited flower-shaped flakes with a width of 20 nm and a length of 700 nm (Figure S19). On the other hand, the TEM and high-resolution TEM (HR-TEM) images showed obvious lattices, suggesting the high crystallinity for these COFs. The HR-TEM images illustrated that a crystal lattice corresponding to the (100), (011), (110) and (100) facets of PYTA-PATA-COF, PYTA-BDTA-COF, PYTA-TDTA-COF and N^+-PYTA-PATA-COF, respectively (Figures 3C-3F and Figures S20-S23). Moreover, energy-dispersive X-ray spectroscopy (EDX) mapping images reveal that all elements (C, N, O) were uniformly distributed in the skeletons of these COFs (Figures S24-S27).
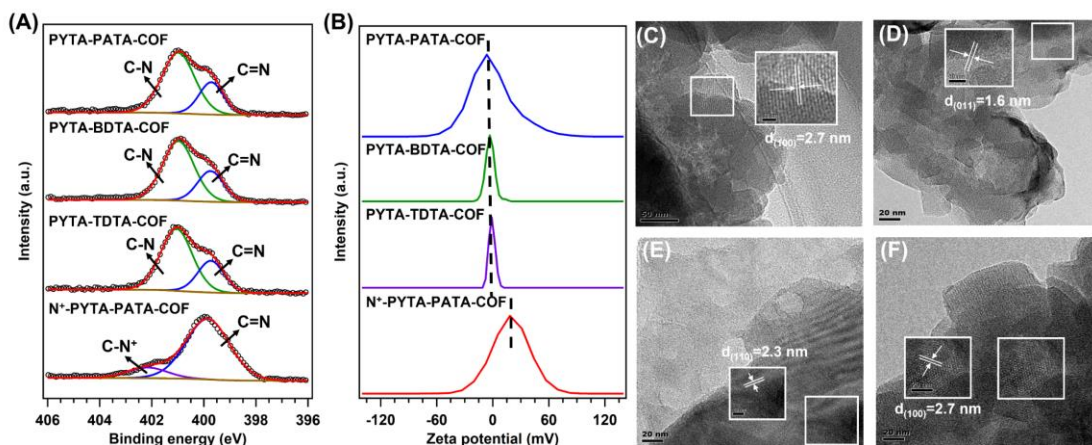
Figure 3. (A) The XPS spectra for N 1s and (B) the Zeta potential curves of PYTA-PATA-COF (blue), PYTA-BDTA-COF (green), PYTA-TDTA-COF (purple) and N^+-PYTA-PATA-COF (red). The HR-TEM images of (C) PYTA-PATA-COF, (D) PYTA-BDTA-COF, (E) PYTA-TDTA-COF and (F) N^+-PYTA-PATA-COF.

The PYTA-PATA-COF, PYTA-BDTA-COF, PYTA-TDTA-COF and N^+-PYTA-PATA-COF with abundant nitrogen atoms and ionic bonds as potential binding sites in the polar skeleton can be developed as ideal platforms for the gold adsorption. The Au ions adsorption behaviors of these COFs were tested at room temperature. The equilibrium curves revealed that the adsorption capacities of PYTA-PATA-COF, PYTA-BDTA-COF, PYTA-TDTA-COF and N^+-PYTA-PATA-COF reached equilibrium when the remaining Au^{3+} concentrations were 845, 850, 588 and 609 mg L^{-1}, respectively (Figure 4A). In addition, we fitted the adsorption curves using the Langmuir and Freundlich adsorption isotherm models (Figure S28-S29). The corresponding parameters were calculated in Table S13, and the Langmuir model had a higher correlation coefficient with these COFs ($R^2 > 0.998$). Therefore, the Langmuir adsorption isotherm model is more acceptable explaining the adsorption performance and illustrate the monolayer adsorption process. Meanwhile, the corresponding maximum gold capture capacities of PYTA-PATA-COF, PYTA-BDTA-COF, PYTA-TDTA-COF and N^+-PYTA-PATA-COF were 1774, 1752, 1880 and 1834 mg g^{-1}, respectively (Figure 4A). To confirm the positive effect of introducing diarylamine units into COFs, we construct the counterpart COF (PYTA-PYTA-COF) without diarylamine units. The PXRD patterns and N_2

adsorption curve showed good crystallinity and pore structure, close to that of PYTA-PATA-COF (Figure S30). However, the equilibrium curves revealed that the adsorption capacity of PYTA-PYTA-COF reach equilibrium when the remaining Au^{3+} concentration was 131.2 mg L^{-1} and the corresponding maximum gold capture capacity was 1144 mg g^{-1}, which is fitted by the Langmuir model (Figure S31). Furthermore, N^+-PYTA-PATA-COF with ionic frameworks reached above 90% of the maximal adsorption capacity within only 10 mins, while the adsorption capacity for PYTA-PATA-COF, PYTA-BDTA-COF and PYTA-TDTA-COF at 10 mins were 55, 45, and 48%, respectively, indicating that the electrostatic interaction between $C-N^+$ bonds and $AuCl_4^-$ anions enhanced the binding rates (Figure 4B). Moreover, the kinetic isotherms of these COFs were fitted through the pseudo-second-order kinetic model with correlation coefficients above 0.997, while the pseudo-first-order kinetic with smaller correlation coefficients were about 0.610-0.845 (Figures S32-S33). The corresponding parameters were calculated in Table S14. Thus, the pseudo-second-order kinetic is more acceptable for demonstrating the adsorption kinetic and exhibit the chemisorption behavior. Notably, the gold capture capacity and kinetics of N^+-PYTA-PATA-COF are higher than that of most reported COFs due to the embedding of electron-rich atoms in the polar skeleton (Table S15). These results further indicated that N^+-PYTA-PATA-COF possesses high adsorption kinetics and removal efficiency for gold ions.
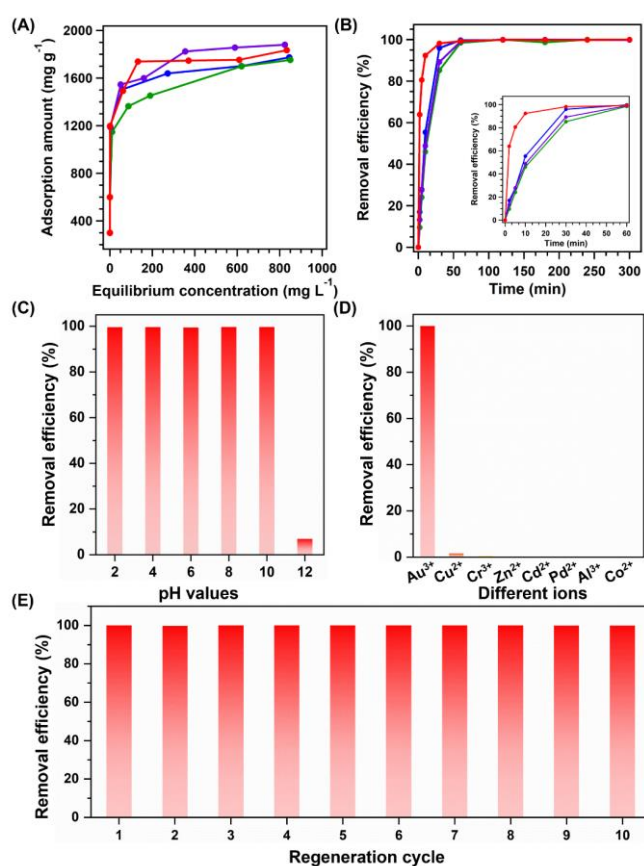
Figure 4. (A) Au^{3+} adsorption isotherms and (B) the remove efficiency of gold ions for PYTA-PATA-COF (blue), PYTA-BDTA-COF (green), PYTA-TDTA-COF (purple) and N^{+}-PYTA-PATA-COF (red) (insert: the removal efficiency within 60 mins). (C) The removal efficiency of Au^{3+} for the N^{+}-PYTA-PATA-COF under different pH conditions. (D) The removal efficiency of Au^{3+} for the N^{+}-PYTA-PATA-COF from the solution of mixed metal ions. (E) The regeneration cycle of N^{+}-PYTA-PATA-COF for the gold capture.

Given that the practical gold capture application is in acid solutions owing to the metal ions of e-wastes requiring digestion by acid solutions, we tested the gold capture efficiency under different pH conditions between pH=2 and pH=12 (Figure 4C). Exactly, the capture efficiency showed about 100% of Au (III) was absorbed in the pH range = 2 to 10, while the uptake activity of N^{+}-PYTA-PATA-COF declined to 12% in the alkaline solution. In addition, the selective extraction of gold in the complex leaching solution containing various competition metal ions (including Cu^{2+}, Cr^{2+}, Zn^{2+}, Cd^{2+}, Al^{3+}, Pd^{2+}, Co^{2+} and Au^{3+}) is important for the practical application. The capture

efficiencies of Cu^{2+}, Cr^{2+}, Zn^{2+}, Cd^{2+}, Al^{3+}, Pd^{2+}, Co^{2+} and Au^{3+} were 1.62%, 0.44%, 0.20%, 0.16%, 0.06%, 0.08%, 0.18% and 97.45%, respectively (Figure 4D). Thus, the ideal selectivity of gold *vs.* other competition metal ions (α) for the N^+-PYTA-PATA-COF can be calculated by $\alpha = EF_{Au}/EF_{ion}$ (EF_i, the capture efficiency) with the values of $\alpha_{Au/Cu} = 61.41$, $\alpha_{Au/Cr} = 226$, $\alpha_{Au/Zn} = 498$, $\alpha_{Au/Cd} = 622$, $\alpha_{Au/Al} = 1658$, $\alpha_{Au/Pd} = 1243$ and $\alpha_{Au/Co} = 553$, respectively.[9b] We investigated the adsorption effect of Hg^{2+} on the Au^{3+} selectivity. As shown in Figure S34, the relative maximum Au^{3+} capture capacity of N^+-PYTA-PATA-COF is 1834 mg g^{-1}, while the relative maximum Hg^{2+} capture capacity is 174 mg g^{-1} at 25 °C under the coexistence of Au^{3+} and Hg^{2+} condition. These results indicated that the Au^{3+} capture showed high selectivity in the coexistence of Au^{3+} and Hg^{2+}.

To confirm the possibility of N^+-PYTA-PATA-COF for the gold capture in real application, the leaching solution was derived from the central processing unit (CPU, containing Cu^{2+}, Fe^{3+}, Ni^{2+}, Zn^{2+}, and Au^{3+} with pH=2). Specifically, the capture efficiency of Cu^{2+}, Fe^{3+}, Ni^{2+}, Zn^{2+}, and Au^{3+} was estimated to be 4.09%, 6.45%, 0.85%, 1.36%, 0.84% and 93.87%, respectively (Figure S35). These results demonstrated that the N^+-PYTA-PATA-COF exhibited an extraordinary ability of gold recovery with high selectivity and capacity, further indicating it could be applied in actual samples. The stability of the gold extraction on N^+-PYTA-PATA-COF is crucial to the practical application. The thiourea solution can easily elute gold ions due to the superior affinity between gold and thiourea; thus, we used thiourea to regenerate the N^+-PYTA-PATA-COF for the next cycle of gold capture. N^+-PYTA-PATA-COF exhibited reliable stability in adsorption-desorption cycling (Figure 4E). It demonstrated a stable adsorption capacity of around 100% each time in the ten cycling rounds, suggesting the excellent reusability of N^+-PYTA-PATA-COF. We selected SO_4^{2-}, CO_3^{2-}, PO_4^{3-}, NO_3^- and Cl^- as the competition ions to evaluate the $AuCl_4^-$ adsorption performance. When the treated solution contained competing anions with the same molar concentration as $AuCl_4^-$, N^+-PYTA-PATA-COF still adsorbed gold ions with high removal efficiencies exceeding 99% (Figure S36).[17] The high affinity for the $AuCl_4^-$ rather than other

competing anions was due to the spontaneous formation of the precipitated Au (0), which promoted binding process and contributed to the high adsorption capacities. In addition, we have calculated the theoretical binding contents of the competing anions (Figure S37). The theoretical binding contents for SO_4^{2-}, CO_3^{2-}, PO_4^{3-}, NO_3^-, Cl^- were 9.1, 5.7, 15.2, 3.9 and 6.7 wt.%, which were 2.0, 1.2, 3.3, 0.8 and 1.4% of the experimental binding contents of $AuCl_4^-$, further confirming its high selectivity among anions.

To further investigate the mechanism of the ultrahigh gold recovery for N^+-PYTA-PATA-COF, we first calculated thermodynamic analysis. The values of Gibbs energy change ($\Delta G < 0$), enthalpy change ($\Delta H > 0$) and entropy change ($\Delta S > 0$) revealed that the adsorption of gold ions for the N^+-PYTA-PATA-COF was (Figure S38 and Table S16). Then, the PXRD patterns also confirm the proceeded spontaneous capture process. The PXRD patterns of N^+-PYTA-PATA-COF disclosed that all peaks from N^+-PYTA-PATA-COF were well retained and new peaks appeared at 38.4, 44.4, 64.7, 77.6 and 81.9 °, attributing to the (111), (200), (220), (311) and (222) facets of Au (0), after just one-minute adsorption, indicating the ultrafast proceeded spontaneously process of reducing Au (III) to Au (0) (Figure 5A). Then, the peaks of N^+-PYTA-PATA-COF were disappeared, and the peak intensity of Au (0) increased after the process of gold recovery within 30 mins. In addition, the PXRD patterns of PYTA-PATA-COF, PYTA-BDTA-COF and PYTA-TDTA-COF after the gold capture also demonstrated the same results, disclosing the proceeded spontaneous capture process (Figures S39-S41). Furthermore, the EDX-mapping images of these COFs also showed the uniform distribution of gold (Figure 5B and Figures S42-S44).
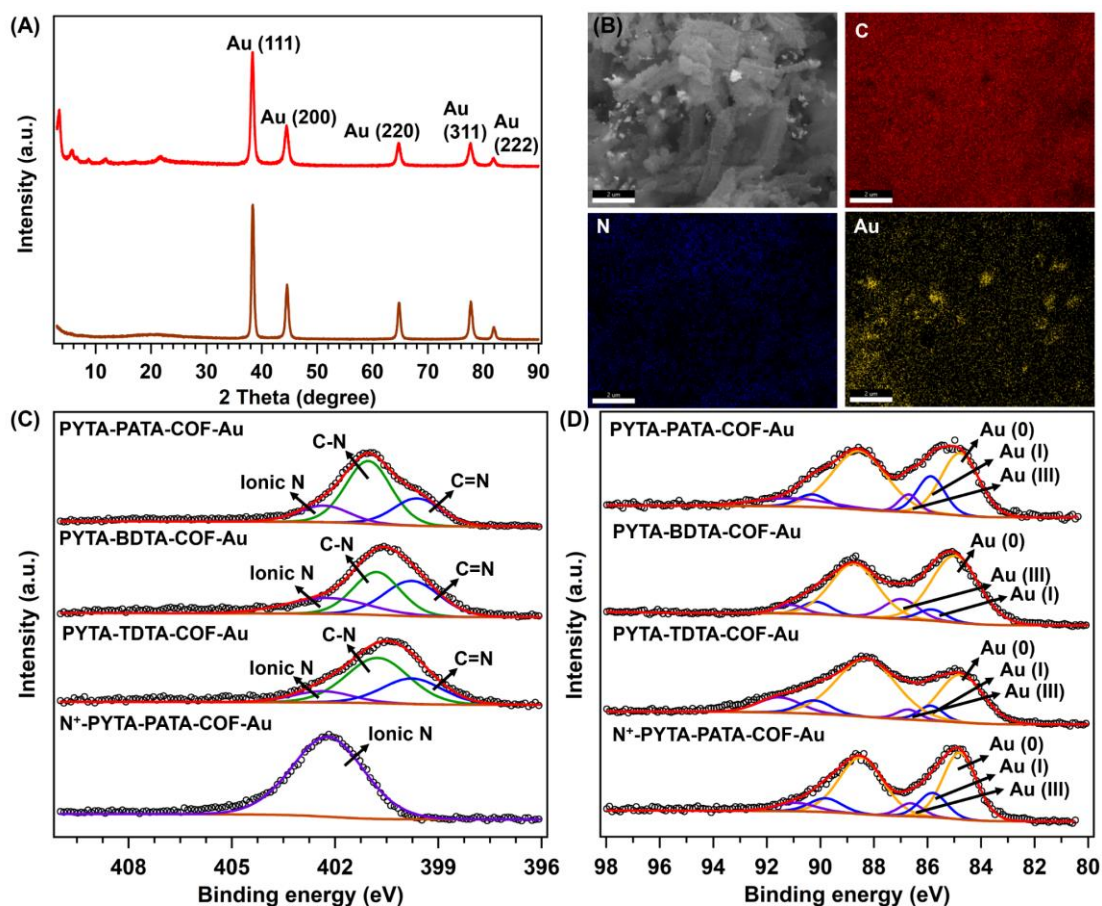
Figure 5. (A) The PXRD patterns of N$^+$-PYTA-PATA-COF after the Au (III) capture within 1 min (red) and 30 mins (brown). (B) The EDX-mapping images of N$^+$-PYTA-PATA-COF after the Au (III) capture. The XPS spectra of (C) N 1s and (D) Au 3f before and after the Au (III) adsorption for PYTA-PATA-COF, PYTA-BDTA-COF, PYTA-TDTA-COF and N$^+$-PYTA-PATA-COF.

Then, we also conducted the XPS spectra of these COFs after the gold capture to explain the states of binding sites and gold ions. The XPS spectra for N 1s of PYTA-PATA-COF, PYTA-BDTA-COF and PYTA-TDTA-COF not only disclosed the existence of C=N and C-N bonds with a binding energy of 399.7 and 400.9 eV, respectively, but also demonstrated a new peak at around 402.33 eV assigning to the C=N$^+$ bonds owing to the protonation in the acidic solution (Figure 5C). Meanwhile, the high resolution of N 1s for the N$^+$-PYTA-PATA-COF remained ionic nitrogen bonds attributed to the ionic skeletons. Thus, we hypothesized that the ionic nitrogen in the polar skeleton after the ionic modification would affect the binding strengths of gold ions, further enhancing

the adsorption efficiency. Furthermore, the high resolution of Au 4f for these COFs suggested that the peaks of Au $4f_{7/2}$ and $4f_{5/2}$ appeared at 84.8 and 88.4 eV assigned to Au (0), 90.2 and 85.7 eV corresponding to Au (I), 91.2 and 86.7 eV contributed to Au (III), respectively (Figure 5D). Notably, the peak intensity of Au (0) was stronger than that of Au (III) and Au (I), revealing that the reduction from Au (III) to gold particles would proceed spontaneously when $AuCl_4^-$ contacted with ionic nitrogen sites. Moreover, the TEM images of N^+-PYTA-PATA-COF-Au also verify this mechanism. Specifically, the TEM images showed that there are many Au particles with different sizes in the range from 60 to 120 nm, suggesting the appearance of the reduction from Au (III) to Au (0) (Figure S45). Thus, redox adsorption is the primary mechanism since Au (III) can be easily reduced to Au (0) by electron-rich COFs and loaded on the frameworks, resulting in the high adsorption capability and selectivity of gold ions over other metal ions.[18]
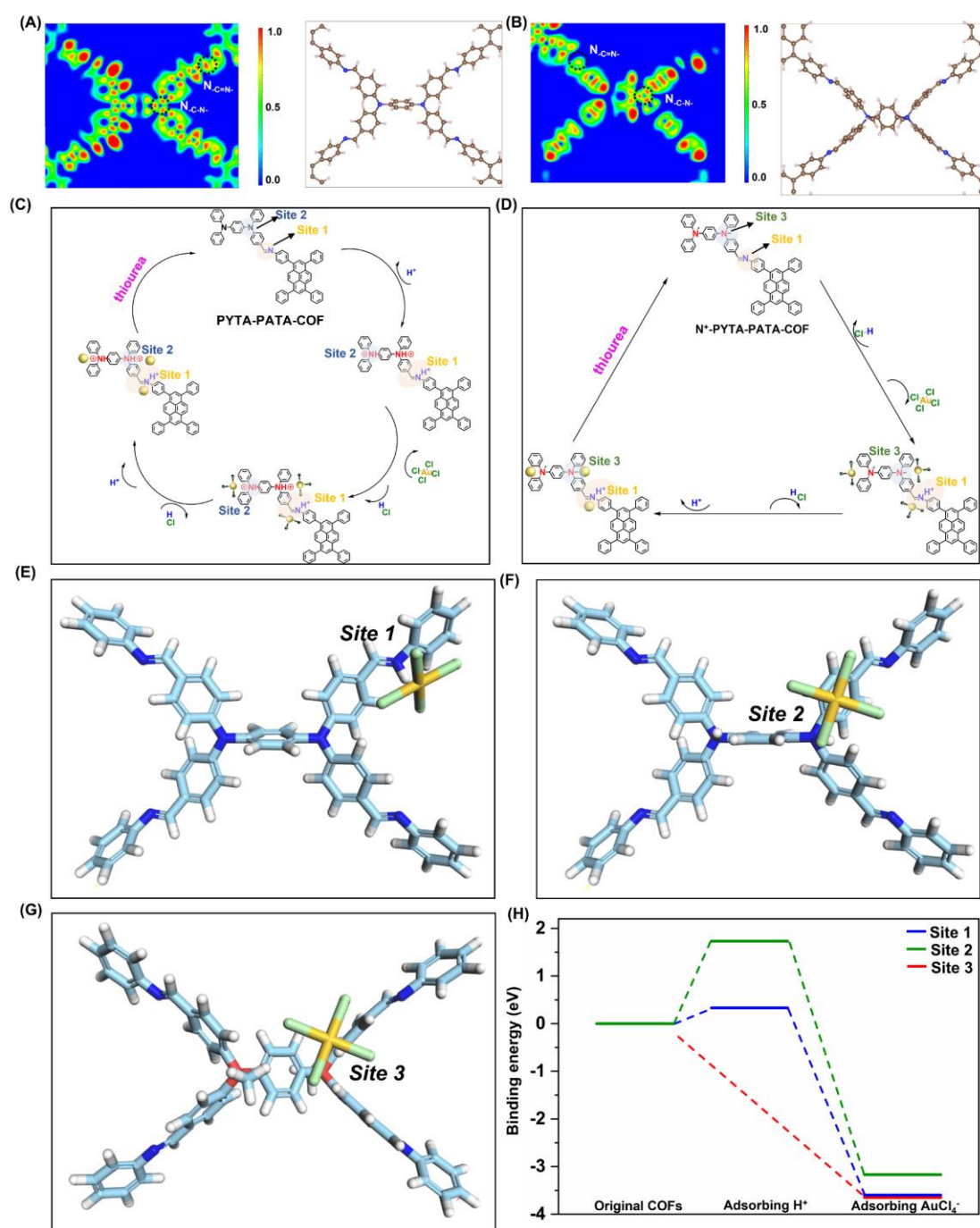
Figure 6. ELF contours and optimized structure for (A) PYTA-PATA-COF and (B) N⁺-PYTA-PATA-COF. The mechanism scheme of gold recovery for (C) PYTA-PATA-COF and (D) N⁺-PYTA-PATA-COF. The optimized structures of adsorbing $AuCl_4^-$ for (E) C=N bonds (*Site 1*), (F) C-N bonds (*Site 2*) and (G) C-N⁺ bonds (*Site 3*). (H) The binding energy profiles of C=N bonds (*Site 1*, blue), C-N bonds (*Site 2*, green) and C-N⁺ bonds (*Site 3*, red) for gold recovery process.

To further study the mechanism of gold recovery over the PYTA-PATA-COF and N⁺-

PYTA-PATA-COF, the DFT calculation was adopted. The electronic localization function (ELF) maps were calculated to investigate the localized electronic distributions of different nitrogen sites. The ELF values of C=N sites are higher than that of C-N sites in the skeleton over the PYTA-PATA-COF, suggesting the highly localized charge density, further indicating the C=N site is a potential electron donor which is beneficial for the proton attack (Figure 6A). Thus, the observation of extra protonated C=N bonds illustrated higher energy consumption of the PYTA-PATA-COF compared with the N^+-PYTA-PATA-COF in the process of gold capture. Furthermore, the lower ELF value of the $C-N^+$ site over the N^+-PYTA-PATA-COF demonstrated that the $C-N^+$ site is a feasible electron acceptor for coordinating with $AuCl_4^-$ ions (Figure 6B).

Thus, we illustrated the adsorption mechanism of gold recovery for these two COFs as below: For the PYTA-PATA-COF, the appearance of protonated C=N (*Site 1*) and C-N (*Site 2*) bonds, which are attacked *via* protons from $HAuCl_4$, is the first step. Then, the protonated C=N and C-N bonds, as the reducing agent, formed the intermediate $AuCl_3^-$ *via* removing Cl^- of $AuCl_4^-$. After that, the Au ions would be reduced to the Au (0) through the spontaneous capture process. Differently, the absence of protonated C=N bonds were observed over the N^+-PYTA-PATA-COF, and the binding site (*Site 3*) was ionic N atoms. Owing to the pre-designable ionic skeletons (Figures 6C and 6D). To better explicit the binding sites in the PYTA-PATA-COF, the binding energies (BEs) of protons for *Site 1* and *Site 2* were obtained at 0.33 and 1.73 eV, respectively, and the smaller BE for *Site 1,* indicating this site was more easily to be preconized. Moreover, the binding energies of $AuCl_4^-$ ions on the different possible binding sites were also calculated. As shown in Figures 6E-6G, the $AuCl_4^-$ ions interacted with the C=N and $C-N^+$ sites of the skeleton over the PYTA-PATA-COF and N^+-PYTA-PATA-COF. The BE values of $AuCl_4^-$ for *Site 1, 2* and *3* were -3.60, -3.17 and -3.65 eV, further demonstrating that ionic amine sites had the stronger binding ability of Au^{3+}, and thus contributed fast capture behavior (Figure 6H). To further verify this pathway, we optimized and calculated the binding energies for directly adsorbing $AuCl_4^-$ for *Site 1*

and *Site 2* on the PYTA-PATA-COF without the protonation process. Specifically, both *Site 1* and *Site 2* sites for the gold ions adsorption exhibited positive values of the binding energy (*Site 1* of 0.49 eV and *Site 2* of 0.22 eV), which were much higher than that of adsorbing $HAuCl_4$ with the protonation process (Figure S46).

We also calculated the water adsorption energy of PYTA-PATA-COF and N^+-PYTA-PATA-COF to determine the competitive adsorption between Au ions and water molecules. For the PYTA-PATA-COF, *Site 1* and *Site 2* bonds as binding sites for the water adsorption. In addition, *Site 1* and *Site 3* bond as binding sites of the N^+-PYTA-PATA-COF for water adsorption. Specifically, the BE values of water for *Site 1* were obtained at -0.12 and -0.28 eV on the PYTA-PATA-COF and N^+-PYTA-PATA-COF, respectively (Figure S47). Meanwhile, the BE values for *Site 2* and *Site 3* were obtained of -0.21 and -0.31 eV on the PYTA-PATA-COF and N^+-PYTA-PATA-COF, respectively (Figure S47). These BEs exhibited smaller values than the Au capture in different sites, suggesting that these binding sites would preferentially adsorb gold ions rather than water molecules.

Conclusion

In summary, a skeleton engineering was demonstrated for constructing COFs with diarylamine derivatives, which can overcome the weak binding ability of the Au ions, as the gold adsorbent with high selectivity and uptakes. The introduction of the ionized skeleton in COFs allowed the establishment of binding sites, contributing to highly capacitive Au capture (1834 mg g^{-1}), high selectivity and superior kinetics (reaching 90% within 10 mins). The experiments and theoretical calculations further revealed that the binding sites altered from C=N bonds to ionic amine sites, thereby forming the coordination with $AuCl_4^-$ via coulomb force, further overleaping the protonation imine bond process and contributing to enhanced absorbing kinetics after the ionization. This work inspired us to design functional skeletons of COFs for ion/molecular capture.

Acknowledgements

Reference

[1] a) F. Li, J. Zhu, P. Sun, M. Zhang, Z. Li, D. Xu, X. Gong, X. Zou, A. K. Geim, Y. Su, H.-M. Cheng, Nat. Commun. 2022, 13, 4472; b) X. Li, Y.-L. Wang, J. Wen, L. Zheng, C. Qian, Z. Cheng, H. Zuo, M. Yu, J. Yuan, R. Li, W. Zhang, Y. Liao, Nat. Commun. 2023, 14, 263.

[2] a) T. S. Nguyen, Y. Hong, N. A. Dogan, C. T. Yavuz, Chem. Mater. 2020, 32, 5343-5349; b) J. Wang, B. Zeng, J. Lv, Y. Lu, H. Chen, ACS Sustain. Chem. Eng. 2020, 8, 16952-16959.

[3] L. M. M. Kinsman, B. T. Ngwenya, C. A. Morrison, J. B. Love, Nat. Commun. 2021, 12, 6258.

[4] a) D. T. Sun, N. Gasilova, S. Yang, E. Oveisi, W. L. Queen, J. Am. Chem. Soc. 2018, 140, 16697-16703; b) J. Cui, L. Zhang, J. Hazard. Mater. 2008, 158, 228-256.

[5] a) Y. Li, W. Chen, G. Xing, D. Jiang, L. Chen, Chem. Soc. Rev. 2020, 49, 2852-2868; b) S. J. Lyle, P. J. Waller, O. M. Yaghi, Trends Chem. 2019, 1, 172-184; c) T. Zhang, G. Zhang, L. Chen, Acc. Chem. Res. 2022, 55, 795-808; d) H.-J. Zhu, M. Lu, Y.-R. Wang, S.-J. Yao, M. Zhang, Y.-H. Kan, J. Liu, Y. Chen, S.-L. Li, Y.-Q. Lan, Nat.

Commun. 2020, 11, 497; d) Z. Liang, H.-Y. Wang, H. Zheng, W. Zhang, R. Cao, Chem. Soc. Rev. 2021, 50, 2540-2581; e) H. Zhang, C. Gu, M.-S. Yao, S. Kitagawa, Adv. Energy Mater. 2022, 12, 2100321.

[6] a) Z. Li, L. Sheng, C. Hsueh, X. Wang, H. Cui, H. Gao, Y. Wu, J. Wang, Y. Tang, H. Xu, X. He, Chem. Mater. 2021, 33, 9618-9623; b) L. Wang, C. Zeng, H. Xu, P. Yin, D. Chen, J. Deng, M. Li, N. Zheng, C. Gu, Y. Ma, Chem. Sci. 2019, 10, 1023-1028; c) M. Liu, S. Yang, X. Yang, C.-X. Cui, G. Liu, X. Li, J. He, G. Z. Chen, Q. Xu, G. Zeng, Nat. Commun. 2023, 14, 3800; d) X. Xu, X. Wu, K. Xu, H. Xu, H. Chen, N. Huang, Nat. Commun. 2023, 14, 3360; e) Y. Yue, H. Li, H. Chen, N. Huang, J. Am. Chem. Soc. 2022, 144, 2873-2878.

[7] a) X. Chen, Y. Li, L. Wang, Y. Xu, A. Nie, Q. Li, F. Wu, W. Sun, X. Zhang, R. Vajtai, P. M. Ajayan, L. Chen, Y. Wang, Adv. Mater. 2019, 31, 1901640; b) M. Liu, S. Yang, S. Liu, Q. Miao, X. Yang, X. Li, Q. Xu, G. Zeng, Small 2022, 2204757; c) M. Kou, Y. Wang, Y. Xu, L. Ye, Y. Huang, B. Jia, H. Li, J. Ren, Y. Deng, J. Chen, Y. Zhou, K. Lei, L. Wang, W. Liu, H. Huang, T. Ma, Angew. Chem. Int. Ed. 2022, 61, e202200413; d) Z. Lei, Q. Yang, Y. Xu, S. Guo, W. Sun, H. Liu, L.-P. Lv, Y. Zhang, Y. Wang, Nat. Commun. 2018, 9, 576; e) Q. Wu, M.-J. Mao, Q.-J. Wu, J. Liang, Y.-B. Huang, R. Cao, Small 2021, 17, 2004933.

[8] a) W. Zhang, L. Chen, S. Dai, C. Zhao, C. Ma, L. Wei, M. Zhu, S. Y. Chong, H. Yang, L. Liu, Y. Bai, M. Yu, Y. Xu, X.-W. Zhu, Q. Zhu, S. An, R. S. Sprick, M. A. Little, X. Wu, S. Jiang, Y. Wu, Y.-B. Zhang, H. Tian, W.-H. Zhu, A. I. Cooper, Nature 2022, 604, 72-79; b) S. An, Q. Xu, Z. Ni, J. Hu, C. Peng, L. Zhai, Y. Guo, H. Liu, Angew. Chem. Int. Ed. 2021, 60, 9959-9963; c) P. Zhang, Z. Wang, S. Wang, J. Wang, J. Liu, T. Wang, Y. Chen, P. Cheng, Z. Zhang, Angew. Chem. Int. Ed. 2022, 61, e202213247; d) X. Liu, F. Gao, T. Jin, K. Ma, H. Shi, M. Wang, Y. Gao, W. Xue, J. Zhao, S. Xiao, Y. Ouyang, G. Ye, Nat. Commun. 2023, 14, 5097.

[9] a) F.-Z. Cui, R.-R. Liang, Q.-Y. Qi, G.-F. Jiang, X. Zhao, Adv. Sustainable Syst. 2019, 3, 1800150; b) Q. Sun, B. Aguila, J. Perman, L. D. Earl, C. W. Abney, Y. Cheng, H. Wei, N. Nguyen, L. Wojtas, S. Ma, J. Am. Chem. Soc. 2017, 139, 2786-2793; c) Q. Fu, T. Zhang, X. Sun, S. Zhang, G. I. N. Waterhouse, C. Sun, H. Li, S. Ai, Chem. Eng.

J. 2023, 454, 140154; d) N. Huang, L. Zhai, H. Xu, D. Jiang, J. Am. Chem. Soc. 2017, 139, 2428-2434; e) W.-R. Cui, C.-R. Zhang, W. Jiang, F.-F. Li, R.-P. Liang, J. Liu, J.-D. Qiu, Nat. Commun. 2020, 11, 436.

[10] J. Qiu, C. Xu, X. Xu, Y. Zhao, Y. Zhao, Y. Zhao, J. Wang, Angew. Chem. Int. Ed. 2023, 62, e202300459.

[11] a) S. Zhong, Y. Wang, T. Bo, J. Lan, Z. Zhang, L. Sheng, J. Peng, L. Zhao, L. Yuan, M. Zhai, W. Shi, Chem. Eng. J. 2023, 455, 140523; b) L. Zhang, Q.-Q. Zheng, S.-J. Xiao, J.-Q. Chen, W. Jiang, W.-R. Cui, G.-P. Yang, R.-P. Liang, J.-D. Qiu, Chem. Eng. J. 2021, 426, 131865.

[12] M. Liu, H.-Y. Kong, S. Bi, X. Ding, G. Z. Chen, J. He, Q. Xu, B.-H. Han, G. Zeng, Adv. Funct. Mater. 2023, 33, 2302637.

[13] a) K. Dutta Dubey, T. Stuyver, S. Kalita, S. Shaik, J. Am. Chem. Soc. 2020, 142, 9955-9965; b) E. M. Arnett, R. Reich, J. Am. Chem. Soc. 1980, 102, 5892-5902; c) J. B. Washington, M. Assante, C. Yan, D. McKinney, V. Juba, A. G. Leach, S. E. Baillie, M. Reid, Chem. Sci. 2021, 12, 6949-6963; d) B. Yang, C. Zhang, ACS Sustainable Chem. Eng. 2022, 10, 9749-9759; e) Y. Song, J.-J. Zhang, Y. Dou, Z. Zhu, J. Su, L. Huang, W. Guo, X. Cao, L. Cheng, Z. Zhu, Z. Zhang, X. Zhong, D. Yang, Z. Wang, B. Z. Tang, B. I. Yakobson, R. Ye, Adv. Mater. 2022, 34, 2110496; f) L.-L. Zhou, Q. Guan, W. Zhou, J.-L. Kan, Y.-B. Dong, Chem. Sci. 2022, 13, 7846-7854.

[14] Deposition Numbers: 2309114, 2309108, 2309115, 2309113 contain the supplementary crystallographic data for this paper. These data are provided free of charge by the joint Cambridge Crystallographic Data Centre and Fachinformationszentrum Karlsruhe Access Structures service.

[15] M. Liu, X. Zhao, S. Yang, X. Yang, X. Li, J. He, G. Z. Chen, Q. Xu, G. Zeng, ACS Appl. Mater. Interfaces 2023, 15, 44384-44393.

[16] M. Liu, S. Liu, C. X. Cui, Q. Miao, Y. He, X. Li, Q. Xu, G. Zeng, Angew. Chem. Int. Ed. 2022, 61, e202213522.

[17] a) J. Cao, Z. Xu, Y. Chen, S. Li, Y. Jiang, L. Bai, H. Yu, H. Li, Z. Bian, Angew. Chem. Int. Ed. 2023, 62, e202302202; b) R. Zhao, D. Chen, N. Gao, L. Yuan, W. Hu, F. Cui, Y. Tian, W. Shi, S. Ma, G. Zhu, Adv. Funct. Mater. 2022, 32, 2200618.

[18]Z. Zhou, W. Zhong, K. Cui, Z. Zhuang, L. Li, L. Li, J. Bi, Y. Yu, Chem. Commun. 2018, 54, 9977-9980.